Density-driven structural transformations in network forming glasses: A high-pressure neutron diffraction study of GeO_2 glass up to 17.5 GPa

Philip S Salmon[1], James W E Drewitt[1,2], Dean A J Whittaker[1], Anita Zeidler[1], Kamil Wezka[1], Craig L Bull[3], Matthew G Tucker[4], Martin C Wilding[5], Malcolm Guthrie[6] and Dario Marrocchelli[7]

[1] Department of Physics, University of Bath, Bath BA2 7AY, UK
[2]CNRS-CEMHTI, University of Orleans, 1d avenue de la Recherche Scientifique, F-45071, Orléans cedex 2, France
[3] SUPA, School of Physics and Centre for Science at Extreme Conditions, University of Edinburgh, Mayfield Road, Edinburgh EH9 3JZ, UK
[4] ISIS Facility, Rutherford Appleton Laboratory, Chilton, Didcot, Oxon OX11 0QX, UK
[5] Institute of Mathematical and Physical Sciences, Aberystwyth University, Aberystwyth SY23 3BZ, UK
[6] Geophysical Laboratory, Carnegie Institution of Washington, Washington, DC 20015, USA
[7] School of Chemistry, Trinity College Dublin, College Green, Dublin 2, Ireland

E-mail: p.s.salmon@bath.ac.uk

Abstract. The structure of GeO_2 glass was investigated at pressures up to 17.5(5) GPa using *in situ* time-of-flight neutron diffraction with a Paris-Edinburgh press employing sintered diamond anvils. A new methodology and data correction procedure were developed, enabling a reliable measurement of structure factors that are largely free from diamond Bragg peaks. Calibration curves, which are important for neutron diffraction work on disordered materials, were constructed for pressure as a function of applied load for both single and double toroid anvil geometries. The diffraction data are compared to new molecular-dynamics simulations made using transferrable interaction potentials that include dipole-polarization effects. The results, when taken together with those from other experimental methods, are consistent with four densification mechanisms. The first, at pressures up to $\simeq$5 GPa, is associated with a reorganization of GeO_4 units. The second, extending over the range from $\simeq$5 to 10 GPa, corresponds to a regime where GeO_4 units are replaced predominantly by GeO_5 units. In the third, as the pressure increases beyond $\sim$10 GPa, appreciable concentrations of GeO_6 units begin to form and there is a decrease in the rate of change of the intermediate-range order as measured by the pressure dependence of the position of the first sharp diffraction peak. In the fourth, at about 30 GPa, the transformation to a predominantly octahedral glass is achieved and further densification proceeds via compression of the Ge-O bonds. The observed changes in the measured diffraction patterns for GeO_2 occur at similar dimensionless number densities to those found for SiO_2, indicating similar densification mechanisms for both glasses. This implies a

regime from about 15 to 24 GPa where SiO_4 units are replaced predominantly by SiO_5 units, and a regime beyond ∼24 GPa where appreciable concentrations of SiO_6 units begin to form.

PACS numbers: 61.43.Fs,61.05.fm,62.50.-p,64.70.kj

1. Introduction

Germania, or GeO_2, is one of a family of 'strong' network glass-forming materials, which includes SiO_2 and BeF_2 [1], whose structures under ambient conditions are based on a relatively open arrangement of corner sharing tetrahedral units with a large mean inter-tetrahedral bond angle $\gtrsim 132^\circ$ [2, 3, 4, 5, 6, 7]. Significant structural changes occur with increasing density [8, 9, 10, 11, 12, 13, 14, 15, 16, 17, 18, 19, 20] and the transformations in germania occur at lower pressures by comparison with silica, making them more amenable to study by different experimental techniques [10, 14, 21]. A prerequisite for understanding the mechanisms of network collapse, and the concomitant changes in the material properties, is unambiguous information on the density dependent structure.

Neutron diffraction has provided a pivotal role in unraveling the mysteries of glassy and liquid materials by providing information that is complementary to x-ray diffraction and, in particular, by enabling the full set of partial structure factors $S_{\alpha\beta}(Q)$ to be separated through application of the isotope substitution method [22]. These $S_{\alpha\beta}(Q)$ functions represent the maximum information on the pair correlation functions that can be extracted from a diffraction experiment in the small-sample limit and, for ambient conditions, they have been successfully measured for several key network glass-forming systems such as GeO_2 [23, 24], $GeSe_2$ [25, 26, 27] and $ZnCl_2$ [28, 29]. Extraction of the partial structure factors does, however, require the measurement of accurate diffraction patterns and this is not an easy task for high-pressure investigations [13] where the sample size is necessarily small and unwanted scattering from the anvils of a press is generally large. Progress has been made in the case of anvils made from cubic BN where the large neutron absorption cross-section of the isotope ^{10}B helps to reduce the background scattering [17, 30, 31]. To achieve larger pressures it is, however, necessary to use anvil materials with a larger compression strength such as sintered diamond for which Bragg scattering and absorption edge effects are generally large, leading to severely contaminated diffraction patterns [32].

In this paper ‡, new *in situ* neutron diffraction results are presented on the structure of GeO_2 glass at pressures increasing to 17.5(5) GPa, thus covering a density range for which there is a substantial progression from a tetrahedral to an octahedral glass. The measured data sets are the highest quality ever obtained above ∼9 GPa, thus enabling a detailed comparison with molecular-dynamics simulations. The experiments were made using the Paris-Edinburgh (PE) press [35] with sintered diamond anvils mounted on the time-of-flight neutron diffractometer PEARL at the ISIS pulsed neutron source. By comparison with previous work [32], the background scattering was reduced considerably by using improved collimation and shielding and a new data correction procedure was developed wherein the diffraction pattern measured for a sample at

‡ The protocol described in this paper for obtaining fully corrected structure factors for glasses at high pressures was erroneously stated to be solely the work of a subset of the present co-authors in Ref. [33]. The record is set straight in a corrigendum [34], and the contributions of the various authors to the present work are outlined in the acknowledgments.

a given pressure is normalized using the diffraction pattern measured for a piece of vanadium compressed to acquire the same geometry as the sample under investigation. In particular, this procedure leads to a first-order cancelation of Bragg peaks arising from the sintered diamond anvils of the press, thus allowing diffraction patterns for glasses and liquids to be measured reliably at pressures beyond 8.5 GPa where (single toroid) cubic BN anvils cannot be dependably used. The diffraction results are compared to new molecular-dynamics simulations made using transferrable interaction potentials that include dipole-polarization effects following the methodology described by Marrocchelli *et al* [36, 37]. The agreement found with experiment supports the occurrence of four densification mechanisms.

The manuscript is organized as follows. The essential theory is given in section 2, the experimental procedure is described in section 3 where pressure calibration curves are presented, and the molecular dynamics method is given in section 4. The new data-reduction method for the *in situ* high-pressure neutron diffraction experiments is then outlined in section 5. This is necessary because the scattering geometry and type of neutron diffraction experiment (time-of-flight pulsed source versus monochromatic reactor source) is *different* to previous work in which accurate structure factors were measured at pressures up to 8.5 GPa [17], the sample-and-anvil geometry is complex, the geometry changes with pressure as the anvils close and the sample and its container deform, and it is not possible to make all of the necessary measurements for the data-reduction at each pressure point. The results are presented in section 6 where, in order to check their veracity, a comparison is made with previous neutron diffraction data for GeO_2 glass taken at pressures up to 8.5 GPa [17]. The results are discussed in section 7 by reference to the findings on the pressure-induced transformations in germania from several diffraction [13, 17, 18], spectroscopic [9, 16, 19] and other simulation [38, 39, 40, 41, 42] methods. A comparison is also made with the results obtained from diffraction experiments on SiO_2 glass at high pressures [15, 20], and the geophysical implications of the results are briefly considered. Concluding remarks are made in section 8.

2. Theory

In a neutron diffraction experiment the scattered intensity containing structural information can be represented by the total structure factor [22]

$$F(Q) = \sum_{\alpha=1}^{n} \sum_{\beta=1}^{n} c_\alpha c_\beta b_\alpha b_\beta \left[S_{\alpha\beta}(Q) - 1 \right] \tag{1}$$

where α and β denote the chemical species, n is the number of different chemical species, c_α and b_α represent the atomic fraction and bound coherent scattering length of chemical species α, $S_{\alpha\beta}(Q)$ is a Faber-Ziman [43] partial structure factor and Q is the magnitude of the scattering vector. The coherent neutron scattering lengths for Ge and O are 8.185(20) and 5.803(4) fm, respectively [44]. For an ionic material the $Q = 0$ limit of

$F(Q)$ is given by [45, 46]

$$F(0) = \langle b \rangle^2 S_{\mathrm{NN}}^{\mathrm{BT}}(0) - \langle b^2 \rangle \tag{2}$$

where the mean coherent scattering length $\langle b \rangle = \sum_\alpha c_\alpha b_\alpha$ and the mean square coherent scattering length $\langle b^2 \rangle = \sum_\alpha c_\alpha b_\alpha^2$. The $Q = 0$ limit of the Bhatia-Thornton [47] number-number partial structure factor is given by $S_{\mathrm{NN}}^{\mathrm{BT}}(0) = \rho k_B T \chi_T$ where ρ is the atomic number density, k_B is the Boltzmann constant, T is the absolute temperature and χ_T is the isothermal compressibility.

The corresponding real space information is provided by the total pair distribution function $G(r)$ which is obtained from the Fourier transform relation

$$\begin{aligned} G(r) &= \frac{1}{2\pi^2 \rho r} \int_0^\infty \mathrm{d}Q\, Q\, F(Q)\, \sin(Qr) \\ &= \sum_{\alpha=1}^{n} \sum_{\beta=1}^{n} c_\alpha c_\beta b_\alpha b_\beta \left[g_{\alpha\beta}(r) - 1 \right] \end{aligned} \tag{3}$$

where r is a distance in real space. The partial pair distribution function $g_{\alpha\beta}(r)$ is related to $S_{\alpha\beta}(Q)$ by the Fourier transform relation

$$g_{\alpha\beta}(r) - 1 = \frac{1}{2\pi^2 \rho r} \int_0^\infty \mathrm{d}Q\, Q\, \left[S_{\alpha\beta}(Q) - 1 \right] \sin(Qr). \tag{4}$$

For r values smaller than the distance of closest approach between the centers of two atoms $g_{\alpha\beta}(r) = g_{\alpha\beta}(r = 0) = 0$ such that, within this low r region, $G(r) = G(r = 0) = -\langle b \rangle^2$. The mean coordination number of atoms of type β, contained in a volume defined by two concentric spheres of radii r_i and r_j centred on an atom of type α, is given by

$$\bar{n}_\alpha^\beta = 4\pi \rho c_\beta \int_{r_i}^{r_j} \mathrm{d}r\, r^2 g_{\alpha\beta}(r). \tag{5}$$

3. Experimental

3.1. Sample preparation

Glassy samples were prepared by first drying ≃5 g of GeO_2 powder (99.9999%, Alfa Aesar), contained in a Pt (10% Rh) crucible, for 2 h at 200 °C. The powder was then melted in air at 1600 °C for 20–30 min after which the crucible was placed on a liquid nitrogen cooled brass block and doused with liquid nitrogen. The crucible was subsequently warmed to room temperature using a heat gun, to avoid condensation of atmospheric water, and the clear glass was then removed as a single piece and stored in a desiccator. The high-pressure experiments used sintered diamond anvils having either a single or double toroid profile, where the latter facilitates access to higher pressures [48, 49]. Both geometries correspond to samples that have a cylindrical core with a spherical cap placed on each flat surface. The uncompressed sample volumes correspond to ≃91.2 mm^3 for the single toroid anvils and ≃33.7 mm^3 for the double toroid anvils. The GeO_2 samples for the single toroid anvil experiments were either in

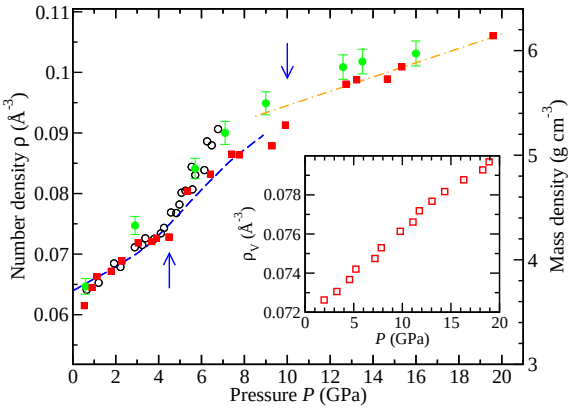

Figure 1. The number density ρ and corresponding mass density for GeO_2 glass as measured on compression from the *in situ* studies of Hong *et al* [50] [(red) ■, no pressure transmitting medium], Smith *et al* [51] (○, 1:1 mixture of pentane and isopentane used as a pressure transmitting medium), Tsiok *et al* [52] (broken (blue) curve, 4:1 mixture of methanol:ethanol used as a pressure transmitting medium with a coated glass sample to avoid reaction with this medium) and Mei *et al* [18] (solid (green) ● with vertical error bars, He pressure transmitting medium). The chained (orange) curve is drawn through the Hong *et al* [50] data points at higher pressures as a guide for the eye and the vertical arrows mark the approximate pressures where there is a change in the gradient $d\rho/dP$. The inset gives the number density of vanadium ρ_V as measured on compression from the *in situ* x-ray diffraction study of Nakamoto *et al* [53] at room temperature [(red) □, He pressure transmitting medium].

the form of a pellet of pre-compacted finely powdered glass or in the form of a solid piece that had been ground to the correct geometry using a rotary tool and polished using diamond paste. The GeO_2 samples for the double toroid anvil experiments were in the form of solid pieces that had been shaped similarly. The pressure P dependence of the number density of GeO_2 glass, as obtained from several *in situ* studies [18, 50, 51, 52], is shown in figure 1. The density values used in the present work were taken from Hong *et al* [50] which are in accord with other studies for several extended pressure ranges. The data sets of Hong *et al* [50], Smith *et al* [51] and Tsiok *et al* [52] all indicate an increase of the gradient $d\rho/dP$ at about 4–5 GPa and the data sets of Hong *et al* [50] and Mei *et al* [18] show a decrease of this gradient at ∼10 GPa. The inset to figure 1 shows the pressure dependence of the number density of vanadium [53].

3.2. Neutron diffraction experiments

The high-pressure experiments were made at room temperature (≃300 K) using the time-of-flight diffractometer PEARL at the ISIS pulsed neutron source. The single and double toroid anvil experiments used a V4 or V3 variant PE press [35] which have piston areas of 100 and 102 cm^2, respectively. The diffractometer views a liquid methane moderator at a temperature of 110 K and the incident and scattered flight paths are 12.6 and 0.6 m, respectively. A transverse scattering geometry was used (figure 2)

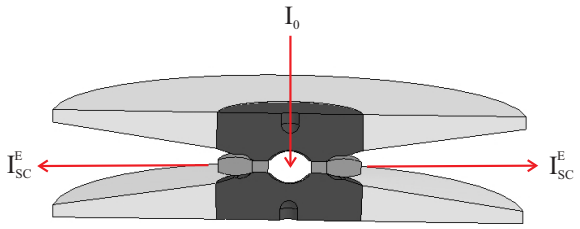

Figure 2. A representation of the transverse scattering geometry for a high-pressure neutron diffraction experiment showing the anvils of the press (dark shading), binding rings (light shading) and Ti-Zr gasket (intermediate shading). The incident beam of intensity I_0 is directed through one of the anvils and the scattered beam of intensity I_{SC}^{E} is observed at an angle $2\theta \simeq 90°$. The illustrated profile is for single toroid anvils.

in which the incident beam is directed along the compression axis through the anvil mounted on the breach of the press and the scattered beam is observed by ^{6}Li-doped ZnS scintillator detectors mounted at a scattering angle 2θ in the range $90\pm7°$. The transmitted beam passes through the second anvil mounted on the piston of the press. Background scattering was reduced by (i) collimating the incident beam using a BN and Gd tube arrangement, where the latter (a cylinder of outer diameter 3.5 mm and wall thickness 0.06 mm) is inserted into the anvil; (ii) by shielding the anvils with neutron absorbing Cd; and (iii), in the case of the single toroid anvil experiments, by inserting neutron absorbing Gd foil of thickness 25 μm between the gaskets and anvils. The background scattering was reduced further by using only those detector pixels encompassing a narrow scattering angle range of $2\theta = 90\pm3.5°$. The sample position changes with the piston displacement upon increasing the applied load. For each pressure point, the press assembly was therefore moved using a motorized system to ensure that the sample was correctly centered in the diffractometer.

For both the single and double toroid anvil geometries, the sample was contained within a standard annular Ti-Zr gasket assembly made from $Ti_{0.676}Zr_{0.324}$ alloy which was chosen because it has an average coherent neutron scattering length of zero. The pressure on the sample was determined from the load L applied to these anvils by constructing calibration curves based on many neutron diffraction experiments using e.g. crystalline systems with a known equation of state in an otherwise identical setup. Such calibration curves are essential for neutron diffraction work on glasses and liquids because the inclusion of a pressure calibrant at the sample position, as used in x-ray diffraction work where high intensity beams can be tightly focussed, will give an undesirable contribution (e.g. Bragg peaks) to the measured intensities.

In the case of single toroid anvils it was found that the calibration curve depends on whether the samples are held in standard or encapsulated [54] Ti-Zr gaskets (figure 3). For this anvil profile, the calibration curve for samples contained in standard Ti-Zr gaskets was deduced from (i) a run in which a pellet made from a 1:3 mixture of NaCl and glassy $GeSe_2$ was compressed in cubic BN anvils, a Rietveld refinement

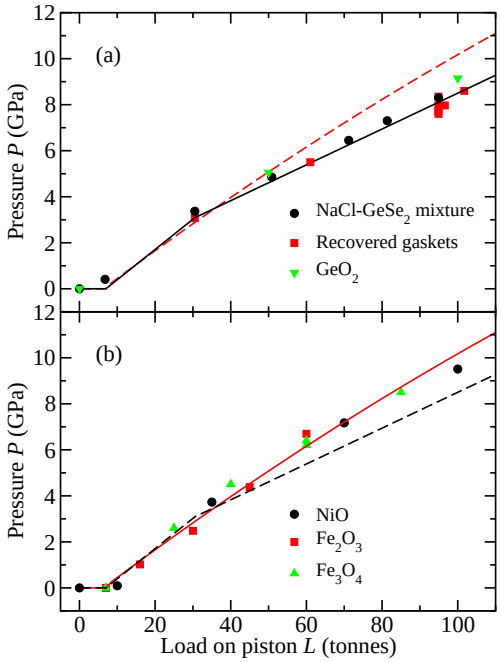

Figure 3. Load L applied to the piston of a V4 or VX5 variant PE press versus the pressure P at the sample position for single toroid anvils at a temperature of $\simeq$300 K. In (a) the data points are for standard Ti-Zr gaskets and correspond to (i) a calibration run using a mixture of NaCl and glassy $GeSe_2$ (•); (ii) measurement of the dimensions of recovered gaskets after various samples were compressed using different loads [(red) ■]; and (iii) consideration of the diamond Bragg peaks measured when various GeO_2 glass pellets were compressed in sintered diamond anvils [(green) ▼]. In (b) the data points are for encapsulated Ti-Zr gaskets [54] and were obtained from the diffraction patterns measured for crystalline NiO (•), Fe_2O_3 [(red) ■] or Fe_3O_4 [(green) ▲]. In (a) the solid calibration curve corresponds to the measured data points and the broken calibration curve corresponds to (b). In (b) the solid calibration curve corresponds to the measured data points and broken calibration curve corresponds to (a).

was made of the NaCl Bragg peaks, and the pressure was obtained from the NaCl equation of state [55]; (ii) applying the procedure described in Ref. [17] where various samples were compressed by different loads using cubic BN anvils and the dimensions of the recovered gaskets were measured; and (iii) compression of GeO_2 glass pellets using sintered diamond anvils where a Rietveld refinement was made of the diamond Bragg peaks and the unit cell volume to pressure conversion was made on the basis of previous experiments on crystalline ice VII [56]. The calibration curve for samples held in encapsulated Ti-Zr gaskets was deduced from the diffraction patterns measured for crystalline NiO [30], Fe_2O_3 (S. Klotz, private communication) or Fe_3O_4 [57] where a 4:1 deuterated methanol-ethanol pressure transmitting medium was used and the samples were compressed using cubic BN anvils.

In the case of double toroid anvils, the available data indicates similar calibration curves for standard and encapsulated Ti-Zr gaskets (figure 4). For this anvil profile, the calibration curve was deduced from (i) the diffraction patterns measured for the

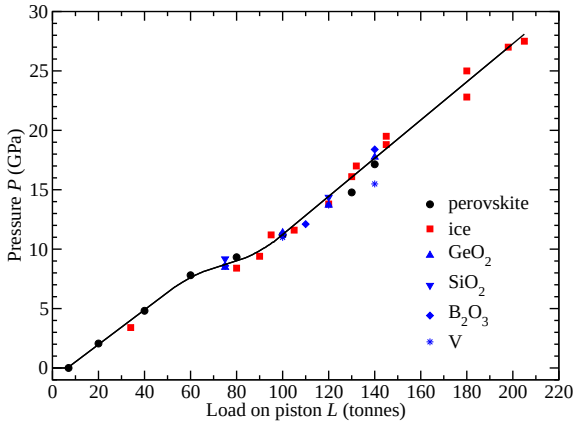

Figure 4. Load L applied to the piston of a V3 variant PE press versus the pressure P at the sample position for double toroid sintered diamond anvils. The calibration curve was deduced from (i) the diffraction patterns measured for a perovskite held in encapsulated Ti-Zr gaskets with a methanol-ethanol-water pressure transmitting medium and a MgO pressure marker (•); (ii) the diffraction patterns measured for crystalline ice held in encapsulated Ti-Zr gaskets [(red) ■]; and (iii) a Le Bail analysis [59] of the Bragg peaks measured for sintered diamond anvils at different pressure points when various samples, contained in standard gaskets, were compressed. For the latter, the unit cell volume to pressure conversion was made on the basis of the perovskite experiment and the data points correspond to samples of GeO_2 [(blue) ▲], SiO_2 [(blue) ▼] or B_2O_3 [(blue) ♦] glass and crystalline vanadium [(blue) ∗]. These data points have been shifted downwards by 2 GPa but show the same P versus L behaviour as for the perovskite and ice samples i.e. although there is an uncertainty in the absolute values of the diamond Bragg peak data points from study (iii) (e.g. the anvils in standard and encapsulated gasket experiments may not be at the same position for the same applied load) their relative values are the same as for studies (i) and (ii).

perovskite $CaSnO_3$ held in encapsulated Ti-Zr gaskets with a MgO pressure marker [58] in a 16:3:1 mixture of deuterated methanol:ethanol:water; (ii) the diffraction patterns measured for crystalline ice held in encapsulated Ti-Zr gaskets; and (iii) a Le Bail analysis [59] of the Bragg peaks measured for sintered diamond anvils at different pressure points when various samples, contained in standard gaskets, were compressed. For the latter, the unit cell volume to pressure conversion was made on the basis of the perovskite experiment.

4. Molecular-dynamics simulations

The molecular-dynamics simulations of the glass were made using the so-called DIPole-Polarizable Ion Model (DIPPIM). In this model, the interaction potentials include dipole-polarization effects and were parameterized by using first principles calculations, and not by using empirical methods, with the aim of developing an accurate and transferrable description of the interactions, going beyond classical pairwise interaction potentials of limited accuracy [36, 60, 61, 62]. For a single set of parameters, the DIPPIM

is the only model that gives a good account of both the structural and vibrational properties of GeO_2 glass at ambient pressure together with the dynamical properties of the liquid at elevated temperatures [36]. The simulations of glassy GeO_2 ($T = 300$ K) were performed using a system of 432 atoms within the NVT ensemble. A time step of 1 fs was used to integrate the equations of motion, and minimization of the polarization energy was carried out at each time step using a conjugate gradient method. The calculations were performed with an in-house code, called PIMAIM.

The glass at ambient pressure was obtained by a procedure where GeO_2 was first liquified at high temperature ($5000-10000$ K) and a 1 ns long run was then made at 4000 K. The system was subsequently cooled down slowly to room temperature, with a cooling rate of ~ 3.7 K/ps, which is nevertheless significantly faster than the experimental ones. The high-pressure states were then obtained by rescaling the cell lengths and particle positions to the new density, making a 1 ns long simulation to equilibrate the system and then another 1 ns run to accumulate enough statistics. This procedure is dubbed cold-compression, see Liang *et al* [63]. The timescale limitations associated with glass compression in the molecular-dynamics simulations §, a problem common to all standard simulation techniques, meant that the equation of state for GeO_2 glass was not reproduced [37]. The new simulations in the present work were therefore made with the density of the glass set at the experimental value used in the diffraction experiments. When necessary, a density to pressure conversion was made using the data of Hong *et al* [50] (figure 1). As shown below, this approach yields very good agreement with the experimental evidence.

5. High-pressure neutron diffraction data-reduction

To a first approximation, the collimation and shielding employed in the diffraction experiments leads to the scattering geometry shown in figure 5 where a cylindrical sample contained within an annular Ti-Zr gasket is illuminated by an incident beam which impinges on the flat face of the sample cylinder. Since the scattering angle is fixed at $2\theta \simeq 90^\circ$, the magnitude of the scattering vector is given by $Q = (4\pi/\lambda)\sin\theta \simeq 2\sqrt{2}\,\pi/\lambda$ and was varied by changing the wavelength λ of the incident beam. In practice, the accessible scattering vector range was $1.55 < Q(\text{Å}^{-1}) \lesssim 19.6$.

Let $I^E_{SC}(Q)$ represent the intensity measured for the sample in its container and let $I^E_B(Q)$ represent the corresponding background intensity, each normalized to the intensity of the incident beam. Then the measured intensity, corrected for background scattering, is given by

$$I_{SC}(Q) = I^E_{SC}(Q) - I^E_B(Q) = a(Q)N_S A_{S,SC}(Q)\frac{d\sigma}{d\Omega}\Big|_S + a(Q)M_{SC}(Q) \qquad (6)$$

where $a(Q)$ is a calibration coefficient which converts cross-sections to measured

§ Experimentally, glasses are also compressed at room-temperature, but they are allowed to equilibrate at the new pressure for much longer times, usually for minutes or hours i.e. there is a difference of $\sim$12 orders of magnitude with respect to the molecular dynmaics simulations.

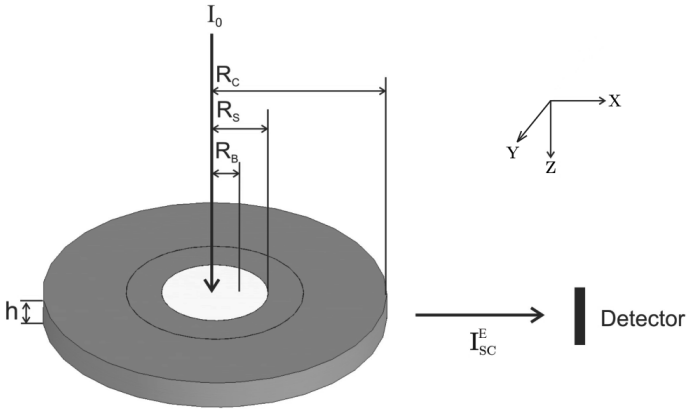

Figure 5. Schematic showing the idealized transverse scattering geometry for a high-pressure neutron diffraction experiment where a sample of radius R_S and height h, contained within an annular gasket of outer radius R_C and height h, is illuminated by a beam of intensity I_0 with a circular profile of radius R_B. The incident beam lies parallel to the Z axis and the scattered beam, of intensity I^E_{SC}, is observed in the X-Y plane.

intensities, N_S is the total number of sample atoms illuminated by the incident beam, $A_{S,SC}(Q)$ is the attenuation coefficient for scattering by the sample and attenuation by the sample and its container (see Appendix A), $M_{SC}(Q)$ is the multiple scattering cross-section for a sample in the presence of its container, and the differential scattering cross-section per sample atom for singly scattered neutrons is given by

$$\left.\frac{d\sigma}{d\Omega}\right|_S = F(Q) + \frac{\sigma_{\text{self}}}{4\pi}. \tag{7}$$

In equation (7) the total structure factor $F(Q)$ is given by equation (1) and the self-scattering cross section σ_{self} is given by

$$\frac{\sigma_{\text{self}}}{4\pi} = \sum_{\alpha=1}^{n} c_\alpha \left(b_\alpha^2 + b_{\text{inc},\alpha}^2\right)\left[1 + P_\alpha(Q)\right] \tag{8}$$

where $b_{\text{inc},\alpha}$ and $P_\alpha(Q)$ are the bound incoherent neutron scattering length and inelasticity correction for chemical species α, respectively.

The calibration coefficient $a(Q)$ for a given pressure can be obtained by replacing the sample by a piece of vanadium and by pressurizing so that it has the same geometry as the sample. Then equations (6) and (7) remain valid, provided the subscript S is replaced by V, such that $I_{VC}(Q) = I^E_{VC}(Q) - I^E_B(Q)$ represents the intensity measured for vanadium in its container after correction for background scattering. The scattering from vanadium is predominantly incoherent i.e. $b_V \simeq 0$ so that equation (7) reduces to $d\sigma/d\Omega|_V = b^2_{\text{inc},V}\left[1 + P_V(Q)\right]$. Equation (6) can then be solved to give $a(Q) = I_{VC}(Q)/\left\{N_V A_{V,VC}(Q)\, b^2_{\text{inc},V}\left[1 + P_V(Q)\right] + M_{VC}(Q)\right\}$ and it follows that

$$\left.\frac{d\sigma}{d\Omega}\right|_S = F(Q) + \frac{\sigma_{\text{self}}}{4\pi} = W(Q)\frac{I_{SC}(Q)}{I_{VC}(Q)} + X(Q) \tag{9}$$

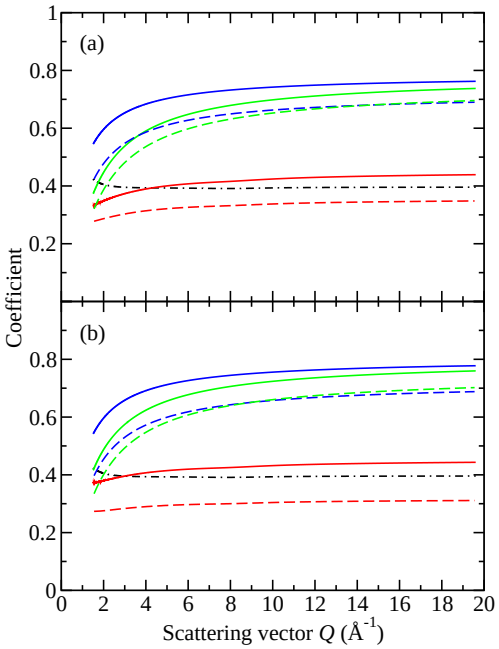

Figure 6. The coefficients $A_{S,SC}(Q)$, $A_{V,VC}(Q)$, and $W(Q)$ (barn) as calculated for (a) single toroid and (b) double toroid anvil geometries at ambient pressure (solid curves) or at a high-pressure corresponding to (a) 8.5 GPa or (b) 17.5 GPa (broken curves). For each panel the set of solid or broken curves represent, in descending order, $A_{S,SC}(Q)$ (blue), $A_{V,VC}(Q)$ (green) and $W(Q)$ (red). Each panel also shows $b^2_{\mathrm{inc},V}\,[1+P_V(Q)]$ (barn) (chained (black) curve). The coefficients $A_{S,SC}(Q)$, $A_{V,VC}(Q)$ and $W(Q)$ were calculated using the dimensions of either the initial or recovered gaskets where the starting sample was in the form of either (a) a compressed powder or (b) a solid piece. The calculations were made for an incident beam of radius $R_B = 0.169$ cm, sample radius R_S of (a) 0.3 cm or (b) 0.2 cm and outer container radius R_C of (a) 0.7335 cm (ambient), 0.9438 cm (8.5 GPa) or (b) 0.69 cm (ambient), 0.895 cm (17.5 GPa). The sample height h was 0.16 cm (ambient), 0.0532 cm (8.5 GPa) or 0.055 cm (17.5 GPa) and the number density of GeO_2 glass at the different pressures is given in table 1. The number densities used for vanadium [53] (see figure 1) and $Ti_{0.676}Zr_{0.324}$ [17] were 0.0721 and 0.0511 Å^{-3} (ambient), 0.0757 and 0.0536 Å^{-3} (8.5 GPa) or 0.0794 and 0.0579 Å^{-3} (17.5 GPa), respectively, where the chosen high-pressure gasket densities are overestimates since they correspond to the pressure of the sample and not to a pressure between that of the sample and ambient. The scattering and absorption cross-sections used in the calculations were taken from Sears [44].

where $W(Q) = \left\{N_V A_{V,VC}(Q)\, b^2_{\mathrm{inc},V}\,[1+P_V(Q)] + M_{VC}(Q)\right\}/N_S A_{S,SC}(Q)$ and $X(Q) = M_{SC}(Q)/N_S A_{S,SC}(Q)$.

To help assess the effect of the different correction factors on the measured $d\sigma/d\Omega|_S$ function, and hence guide in the analysis of the measured data sets, the attenuation factors $A_{S,SC}(Q)$ and $A_{V,VC}(Q)$ were calculated using the procedure described in Appendix A for the geometry shown in figure 5 and the inelasticity corrections $P_\alpha(Q)$ were calculated using the procedure described in Ref. [64]. An order of magnitude estimate of the multiple scattering cross-sections $M_{SC}(Q)$ and $M_{VC}(Q)$ was made using

the procedure described in Ref. [65]. In these calculations the pressure dependence of the number densities of vanadium and $Ti_{0.676}Zr_{0.324}$ were taken from Ref. [53] (see figure 1) and Ref. [17], respectively. The results indicate that the contribution of $M_{VC}(Q)$ to $W(Q)$ is small (1−2% depending on the geometry) and that $X(Q) \ll \sigma_{\rm self}/4\pi$ such that, at a given pressure point, equation (9) can be re-written as

$$F(Q) \simeq W(Q) I_{SC}(Q)/I_{VC}(Q) - \sigma_{\rm self}/4\pi. \tag{10}$$

For comparable sample and vanadium volumes it follows that $W(Q) \simeq \rho_V A_{V,VC}(Q)\, b^2_{{\rm inc},V}\, [1 + P_V(Q)]\, /\rho_S A_{S,SC}(Q)$ where ρ_S and ρ_V are the atomic number densities of the sample and vanadium, respectively. Typical examples of the functions $A_{S,SC}(Q)$, $A_{V,VC}(Q)$ and $W(Q)$ for single and double toroid anvil geometries at both ambient and high-pressure are given in figure 6. The results show that $W(Q)$ is a weakly varying function of Q and is relatively flat at high Q values.

In our PEARL experiments, the intensity $I^E_C(Q)$ was first measured for an empty uncompressed gasket (container) at ambient pressure where the beam radius is smaller than the inner gasket radius so that the latter is not directly illuminated. The intensity was then measured for the GeO_2 sample in its container $I^E_{SC}(Q)$ at each pressure point as the glass was progressively compressed. Finally, the intensity was measured for a piece of vanadium in its container $I^E_{VC}(Q)$ which was compressed to match the sample geometry at each pressure point. The bulk modulus at ambient pressure and temperature is 157.12 GPa for vanadium [66] and 24 GPa for GeO_2 glass [51, 67]. It is therefore anticipated that different loads will be required in order to achieve the same volume and scattering geometry for these materials. In practice, for each intensity $I^E_{SC}(Q)$ measured for a given load, a smaller load was first chosen for vanadium. A short measurement of $I^E_{VC}(Q)$ was made and the data were analyzed (see below). If necessary, the load on vanadium was then increased and the process repeated until the ratio of the background corrected intensities $I_{SC}(Q)/I_{VC}(Q)$ was roughly constant at high Q values.

The data sets $I^E_{SC}(Q)$ and $I^E_{VC}(Q)$ measured for GeO_2 glass at the highest pressure point using single toroid anvils are shown in figure 7(a), together with the background intensity $I^E_C(Q)$ measured with an empty gasket under ambient conditions. In practice, the background intensities for $I^E_{SC}(Q)$ and $I^E_{VC}(Q)$ at each pressure point cannot be measured and they were taken to be scaled versions of $I^E_C(Q)$ with Q independent scaling factors chosen to minimize the diamond Bragg peak intensities in the ratio $I_{SC}(Q)/I_{VC}(Q)$ (figure 7(b)). The geometry at each pressure point is uncertain and, on account of the anvil profiles, it does not correspond to a perfect cylindrical sample. Additionally, the scattering geometry used on the PEARL diffractometer means that the region $Q \leq 1.55$ Å^{-1} is not accessible to the diffraction experiments which is especially inconvenient at lower pressures since the diffraction patterns have a so-called first sharp diffraction peak (FSDP) at $Q \simeq 1.5$ Å^{-1} [23, 24]. An iterative data analysis procedure was therefore developed using, as a starting point, the diffraction patterns measured over an extended Q range for which the FSDP appears in full [23, 24]. Manipulation of these data sets showed that it is necessary to make a plausible extrapolation of the

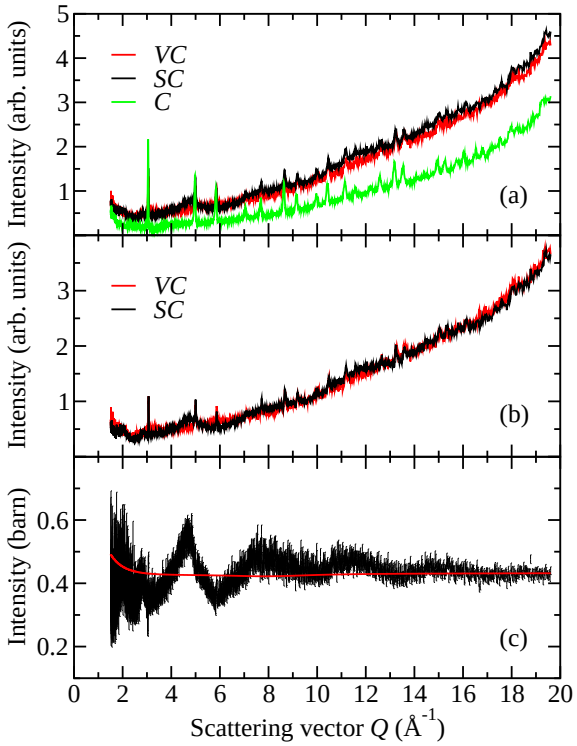

Figure 7. The intensities measured using PEARL, with a PE press and single toroid sintered diamond anvils, together with the first steps in the data analysis procedure used to obtain the total structure factor $F(Q)$ for GeO_2 glass at a pressure of 8.5(5) GPa. (a) The intensities $I^E_{SC}(Q)$, $I^E_{VC}(Q)$ and $I^E_C(Q)$ measured for piston loads L of 100, 110 and 2 tonnes, respectively, where a small Q binning is used in order to maintain the sharpness of the Bragg peaks and aid in their subtraction. The slopes on the data sets arise from background scattering which increases with Q because the Cd shielding on the anvils and on the secondary collimation before the detectors becomes less effective with increasing neutron energy. (b) The background corrected intensities $I_{SC}(Q) = I^E_{SC}(Q) - aI^E_C(Q)$ and $I_{VC}(Q) = I^E_{VC}(Q) - bI^E_C(Q)$ where the constant scaling factors a and b were chosen to minimize the Bragg peak intensities in the ratio $I_{SC}(Q)/I_{VC}(Q)$. (c) The points with vertical error bars show the ratio $W(Q)I_{SC}(Q)/I_{VC}(Q)$ (see equation (10)), where $W(Q)$ is taken to be a Q independent scaling factor, and the solid light (red) curve shows the self-scattering limit $\sigma_{\rm self}/4\pi$ calculated using equation (8).

PEARL data sets to small Q values in order to ensure that the corresponding r space function has the expected small r behavior.

In the iterative data analysis procedure, $W(Q)$ is taken to be a Q independent scaling factor which is chosen so that $W(Q)I_{SC}(Q)/I_{VC}(Q)$ oscillates around the self-scattering limit $\sigma_{\rm self}/4\pi$ as calculated using equation (8) (figure 7(c)). The zeroth approximation for the total structure factor $F^{(0)}(Q)$ is then calculated by using equation (10) and the region for $Q \leq 1.55$ Å^{-1} is set to the $Q = 0$ limit as estimated e.g. from the sample compressibility (section 2). The corresponding total pair distribution function $G^{(0)}(r)$ is found using equation (3) and large amplitude

features in $G^{(0)}(r)$, below the distance of closest approach between two atoms, are set to the calculated $r = 0$ limit (section 2). The resultant data set is then back Fourier transformed to give a revised total structure factor $F^{(1)}(Q)$. The low Q region of the latter is fitted with a Lorentzian function, since this often gives a good account of the FSDP [68, 69], such that the fitted function passes through the expected $Q = 0$ limit. The revised $F^{(1)}(Q)$ function is then Fourier transformed to give $G^{(1)}(r)$, large amplitude features in $G^{(1)}(r)$ below the distance of closest approach between two atoms are set to the calculated $r = 0$ limit, and the resultant data set is back Fourier transformed to give a revised total structure factor $F^{(2)}(Q)$. The latter is then scaled, the small Q region is refitted with a Lorentzian and the entire procedure is re-iterated until, as far as possible, (i) the small r oscillations in the final $G(r)$ function are of minimal amplitude and are symmetrical about the calculated limit $G(0) = -\langle b \rangle^2$ and (ii) there is agreement between the final $F(Q)$ function and the back Fourier transform of the final $G(r)$ function after any large amplitude features below the distance of closest approach between two atoms are set to the calculated $G(0)$ limit.

6. Results

The efficacy of our data correction procedure was tested by comparing the measured $F(Q)$ functions for GeO_2 glass from several independent experiments where these are available for pressures $\lesssim$8.5 GPa. As shown in figure 8, the results obtained from PEARL using either single or double toroid sintered diamond anvils are essentially free from diamond Bragg peaks and the $F(Q)$ functions measured for these anvil geometries at ambient pressure or at 8.5(5) GPa are in agreement within the statistical error. These data sets, and the $F(Q)$ function measured using PEARL with single toroid sintered diamond anvils at 4.5(5) GPa, are in agreement with the $F(Q)$ functions measured at similar pressures using the diffractometer D4C with a monochromatic incident beam at the reactor neutron source of the Institut Laue-Langevin [17]. In these D4C experiments a PE press with single toroid cubic BN anvils was employed in a *different* scattering geometry to PEARL, with the incident and scattered beams in the same plane, such that a *different* data analysis procedure had to be used. The maximum pressure that can be dependably achieved by using these single toroid cubic BN anvils is ∼8.5 GPa. The ambient pressure data sets are also in agreement with the $F(Q)$ function measured for GeO_2 glass held within a standard vanadium container using a geometry in which the low angle detector banks on PEARL were accessible. This experiment gave access to small Q values, enabling the FSDP to be measured in full.

The full set of total structure factors $F(Q)$, measured using PEARL with either single or double toroid sintered diamond anvils at pressures up to 17.5(5) GPa, is shown in figures 9 and 10. With increasing pressure, there is a reduction in height of the FSDP and a shift in its position to higher Q values, accompanied by an enhancement of the principal peak which also shifts position to higher Q values (table 1). In comparison, x-ray diffraction results for a similar pressure range also show a shift of the FSDP to

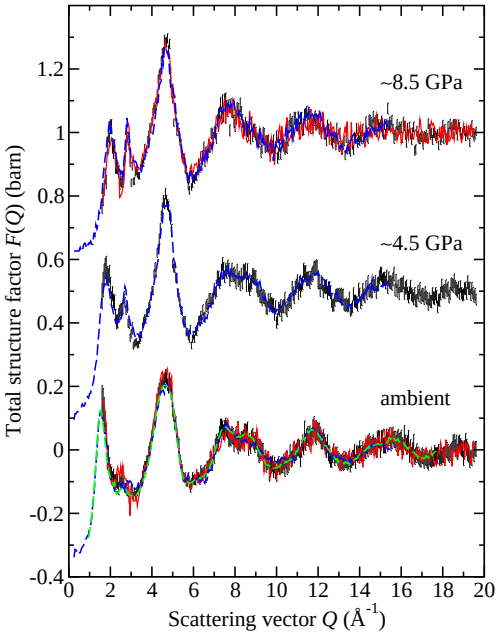

Figure 8. The total structure factor $F(Q)$ as measured by neutron diffraction for GeO_2 glass at different pressures. The points with vertical (black) error bars show the results obtained by using the diffractometer PEARL with the PE press and single toroid sintered diamond anvils at ambient pressure, 4.5(5) and 8.5(5) GPa. The solid light (red) curves show the results obtained by using PEARL with the PE press and double toroid sintered diamond anvils at ambient pressure and 8.5(5) GPa. The broken dark (blue) curves show the results obtained by using the diffractometer D4C with the PE press and single toroid cubic BN anvils in a different geometry to PEARL at ambient pressure, 4.9(5) and 8.0(5) GPa [17]. The broken light (green) curve shows the result obtained at ambient pressure by using PEARL with the sample held in a vanadium container and mounted so that the detectors at scattering angles of $\simeq$90° and 20−60° could all be used. The data sets for pressures larger than ambient are displaced vertically for clarity of presentation.

higher Q values but the principal peak, which is a notable feature at ambient pressure, merges with the FSDP and disappears at pressures $\lesssim$ 7.4 GPa [18]. This variation of behavior can be attributed to the different weighting factors for the partial structure factors in $F(Q)$ for neutron and x-ray diffraction experiments, where the Ge-Ge, Ge-O and O-O weighting factors are in the ratio 0.1710:0.4851:0.3439 for the former and 0.4444:0.4444:0.1111 for the latter at $Q = 0$ [24]. For example, the sharpening of the principal peak in the $F(Q)$ function measured by neutron diffraction with increasing pressure is likely to arise from an enhancement of the principal peak in $S_{\mathrm{GeGe}}(Q)$ and/or $S_{\mathrm{OO}}(Q)$ relative to the principal trough in $S_{\mathrm{GeO}}(Q)$ (see figure 10 in Ref. [24]).

The full set of total pair distribution functions $G(r)$ is shown in figures 11 and 12. The first peak is attributed to Ge-O correlations [24] and the mean bond length and coordination number that it provides for the various pressures are listed in table 1. The results show a broadening of the first peak which shifts position to larger r values when the pressure exceeds a threshold value of $\simeq$4.5(5) GPa, accompanying a steady increase

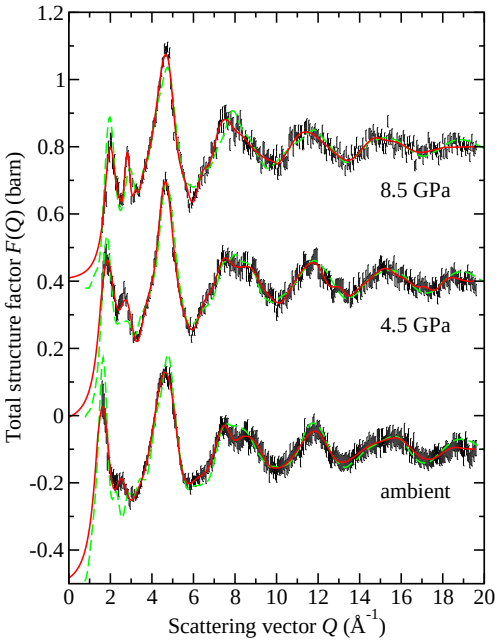

Figure 9. The total structure factor $F(Q)$ as measured for GeO_2 glass at different pressures using a PE press with single toroid sintered diamond anvils. The measured data sets correspond to the points with vertical error bars and the spline fits to these data sets are given by the solid (red) curves. The region $Q \leq 1.55$ Å^{-1} was not accessible in the diffraction experiments and the solid (red) curves within this region correspond to fitted Lorentzian functions (see the text). The broken (green) curves show the molecular dynamics results obtained by using the DIPPIM interaction potentials. The data sets are displaced vertically for clarity of presentation.

in the Ge-O coordination number from $\bar{n}^{\rm O}_{\rm Ge} = 4.2(2)$ at 4.5(5) GPa to $\bar{n}^{\rm O}_{\rm Ge} = 5.5(2)$ at 17.5(5) GPa. This threshold corresponds to a pressure where there is an increase in the rate of change of the glass density with pressure (figure 1). As shown in table 1, the ratio $r_2/r_{\rm GeO}$ decreases with increasing pressure where r_2 is the position of the second peak in $G(r)$. This is consistent with a decrease in the ratio of $r_{\rm OO}/r_{\rm GeO}$ from the value of $\sqrt{8/3} = 1.633$ expected for tetrahedral GeO_4 motifs to the value of $\sqrt{2}$ expected for octahedral GeO_6 motifs.

7. Discussion

7.1. Comparison with other experimental results

The FSDP is associated with intermediate-range order of periodicity given by $2\pi/Q_{\rm FSDP}$, where $Q_{\rm FSDP}$ is the peak position, and a correlation length related to the inverse of the peak width [69]. The pressure dependence of the FSDP position found from the present neutron diffraction work is compared in figure 13 to the results obtained from the *in situ* neutron diffraction experiments of Drewitt *et al* [17] and the *in situ* x-ray diffraction

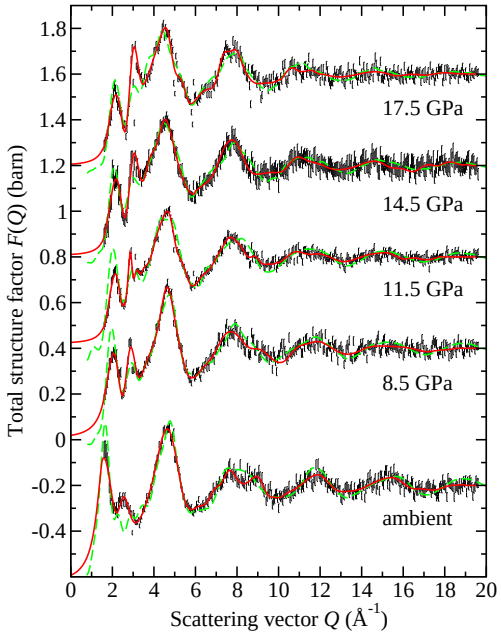

Figure 10. The total structure factor $F(Q)$ as measured for GeO_2 glass at different pressures using a PE press with double toroid sintered diamond anvils. The measured data sets correspond to the points with vertical error bars and the spline fits to these data sets are given by the solid (red) curves. The region $Q \leq 1.55$ Å^{-1} was not accessible in the diffraction experiments and the solid (red) curves within this region correspond to fitted Lorentzian functions (see the text). The broken (green) curves show the molecular dynamics results obtained by using the DIPPIM interaction potentials. The data sets are displaced vertically for clarity of presentation.

experiments of Guthrie *et al* [13]‖, Hong *et al* [50] and Mei *et al* [18]. The individual data sets show a more-or-less linear increase of $Q_{\rm FSDP}$ with pressure until a value of $\sim$10 GPa is reached, whereupon the gradient decreases. This pressure point also marks a decrease in the rate of change of the glass density with pressure (figure 1) and it corresponds to a modification in the main features observed with increasing pressure in x-ray absorption near-edge spectroscopy (XANES) and extended x-ray absorption fine structure (EXAFS) spectroscopy experiments on GeO_2 glass [19]. A bifurcation of the pressure dependence of $Q_{\rm FSDP}$ is also observed at pressures $\gtrsim$8 GPa, with the x-ray diffraction data of Mei *et al* [18] giving larger peak positions at a given pressure by comparison with the present neutron diffraction data and the x-ray diffraction data of Guthrie *et al* [13] and Hong *et al* [50]. The reason for this discrepancy may lie with the fact that, unlike the other experiments, the x-ray diffraction work of Mei *et al* [18] was made using helium as a pressure transmitting medium to promote hydrostatic conditions. If the latter is responsible for the bifurcation then the behavior is in contrast

‖ The FSDP positions from Ref. [13] reported in figure 13 were taken either from the peak maximum in $S(Q)$ or, at pressures > 7 GPa where the peak is not resolved, by identifying the leading edge of the FSDP and assuming the same width as the FSDP at 6−7 GPa. The positions differ from those reported in Ref. [18].

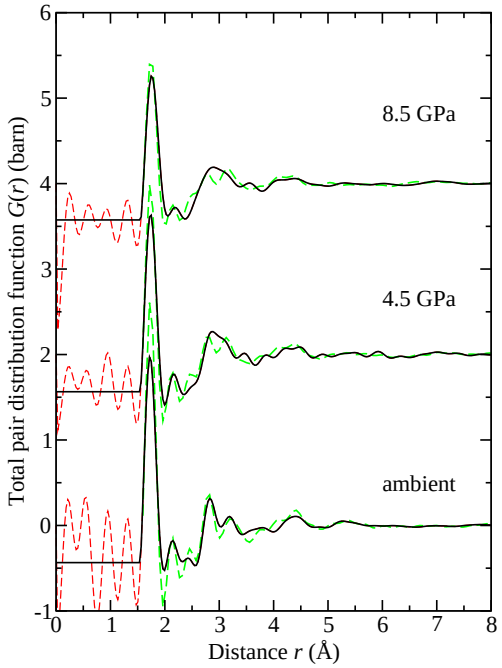

Figure 11. The total pair distribution function $G(r)$ for GeO_2 glass at different pressures as measured using single toroid sintered diamond anvils. The solid (black) curves were obtained by Fourier transforming the corresponding $F(Q)$ functions given by the solid (red) curves in figure 9 and the broken (red) curves show the extent of the unphysical oscillations at r values smaller than the distance of closest approach between the centers of two atoms. The broken (green) curves show the molecular dynamics results obtained by using the DIPPIM interaction potentials. The latter were obtained by truncating the simulated $F(Q)$ functions at the experimental value $Q_{\max} = 19.6$ Å^{-1} and Fourier transforming. The data sets for pressures larger than ambient are displaced vertically for clarity of presentation.

to SiO_2 glass where He can enter voids in the network structure and thereby reduce the compressibility [70, 71]. Further investigations on the effect of He would be interesting because the behavior of the FSDP reflects the collapse of the intermediate-range order with increasing density and the bifurcation occurs at the start of a pressure regime where molecular-dynamics simulations predict the formation of octahedral GeO_6 units (see section 7.2).

The pressure dependence of the Ge-O bond length and coordination number found in the present work are compared in figure 14 to the results obtained from other neutron and x-ray diffraction and EXAFS spectroscopy experiments [13, 16, 17, 18, 19]. The results show that the Ge atoms remain four-fold coordinated until a threshold pressure of $\simeq$5 GPa is attained i.e. the density within this regime increases predominantly via a reorganization of corner sharing tetrahedral GeO_4 motifs [10, 17, 21]. At higher pressures the Ge-O bond length steadily increases as the coordination shell of germanium expands to incorporate a larger number of nearest neighbor oxygen atoms. The threshold pressure of 5 GPa also marks a change in the pressure dependence of the principal peak position

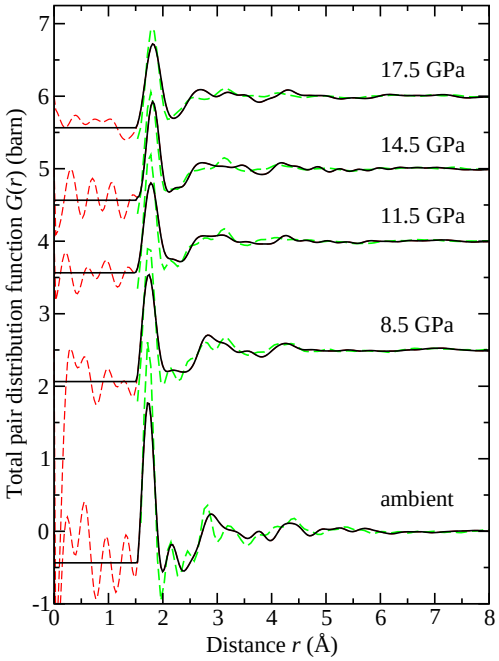

Figure 12. The total pair distribution function $G(r)$ for GeO_2 glass at different pressures as measured using double toroid sintered diamond anvils. The solid (black) curves were obtained by Fourier transforming the corresponding $F(Q)$ functions given by the solid (red) curves in figure 10 and the broken (red) curves show the extent of the unphysical oscillations at r values smaller than the distance of closest approach between the centers of two atoms. The broken (green) curves show the molecular dynamics results obtained by using the DIPPIM interaction potentials. The latter were obtained by truncating the simulated $F(Q)$ functions at the experimental value $Q_{\max} = 19.6$ Å^{-1} and Fourier transforming. The data sets for pressures larger than ambient are displaced vertically for clarity of presentation.

in the Raman spectrum of GeO_2 glass [50]. There is no indication of an abrupt change in the Ge-O bond length at pressures between 6.6 and 8.0 GPa, as reported in a previous EXAFS experiment [9], nor of a plateau region between 6 and 10 GPa where $\bar{n}^{\rm O}_{\rm Ge} \simeq 5$ [13]. The majority of the experimental results illustrated in figure 14(b) indicate that a pressure in excess of 18 GPa is necessary in order to form a fully octahedral glass for which $\bar{n}^{\rm O}_{\rm Ge} = 6$. Recent EXAFS results suggest that the latter is achieved when the pressure is about 30 GPa [19].

7.2. Comparison with molecular dynamics results

As shown in figures 9–12, the molecular-dynamics simulations made using the DIPPIM interaction potentials (section 4) reproduce the main features of the measured $F(Q)$ and $G(r)$ functions although, at the highest pressure points, there is a tendency to underestimate the sharpness of the principal peak in $F(Q)$ and the position of the first peak maximum in $G(r)$. The molecular dynamics results do, however, show a growing asymmetry of the first peak in $g_{\rm GeO}(r)$ with increasing pressure and the weighted

Table 1. Several parameters describing the pressure dependence of the structure of GeO_2 glass as obtained from neutron diffraction experiments using PEARL with either single toroid (ST) or double toroid (DT) sintered diamond anvils. The number density ρ of the glass [50] is given together with the position $Q_{\rm FSDP}$ of the first sharp diffraction peak, the position $Q_{\rm PP}$ of the principal peak, the Ge-O bond distance $r_{\rm GeO}$ taken from the position of the first peak in $G(r)$, the mean Ge-O coordination number $\bar{n}^{\rm O}_{\rm Ge}$, and the ratio $r_2/r_{\rm GeO}$ where r_2 is the position of the second peak in $G(r)$.

Pressure (GPa)	Anvils	ρ (Å^{-3})	$Q_{\rm FSDP}$ (Å^{-1})	$Q_{\rm PP}$ (Å^{-1})	$r_{\rm GeO}$ (Å)	$\bar{n}^{\rm O}_{\rm Ge}$	$r_2/r_{\rm GeO}$
Ambient	ST	0.0629(3)	1.63(5)	2.51(3)	1.73(2)	4.0(2)	1.636
Ambient	DT	0.0629(3)	1.59(5)	2.56(3)	1.73(2)	3.9(2)	1.671
4.5(5)	ST	0.0761(9)	1.86(3)	2.73(3)	1.74(2)	4.2(2)	1.649
8.5(5)	ST	0.0868(9)	2.01(3)	2.82(3)	1.76(2)	4.7(2)	1.642
8.5(5)	DT	0.0868(9)	2.06(3)	2.90(3)	1.75(2)	4.5(2)	1.617
11.5(5)	DT	0.0951(9)	2.14(3)	2.87(3)	1.78(2)	4.8(2)	1.545
14.5(5)	DT	0.0987(9)	2.18(3)	3.07(3)	1.81(2)	5.0(2)	1.492
17.5(5)	DT	0.1031(9)	2.17(3)	3.06(3)	1.82(2)	5.5(2)	1.462

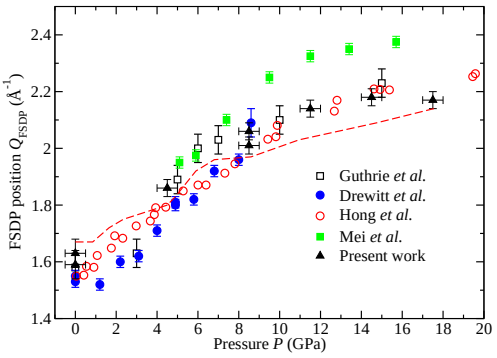

Figure 13. Pressure dependence of the FSDP position, $Q_{\rm FSDP}$, for GeO_2 glass as obtained from the *in situ* neutron diffraction studies of Drewitt *et al* [17] [(blue) ●] and the present work (▲) or from the *in situ* x-ray diffraction studies of Guthrie *et al* [13] (□), Mei *et al* [18] [(green) ■] and Hong *et al* [50] [(red) ○]. The broken (red) curve shows the molecular dynamics results obtained by using the DIPPIM interaction potentials taken from the first peak in $F(Q)$ as calculated for neutron diffraction using equation (1).

peak position $\langle r_{\rm GeO}\rangle = \int dr\, r g_{\rm GeO}(r) / \int dr\, g_{\rm GeO}(r)$ follows the neutron diffraction results (figure 14). The simulations also show a threshold pressure of ≃4.5 GPa below which the Ge-O bond length and coordination number remain constant (figure 14) and where compaction occurs via a change in the intermediate-range order as reflected by the pressure dependence of $Q_{\rm FSDP}$ (figure 13). At pressures greater than this threshold, the simulation results for the Ge-O bond length and coordination number again mimic

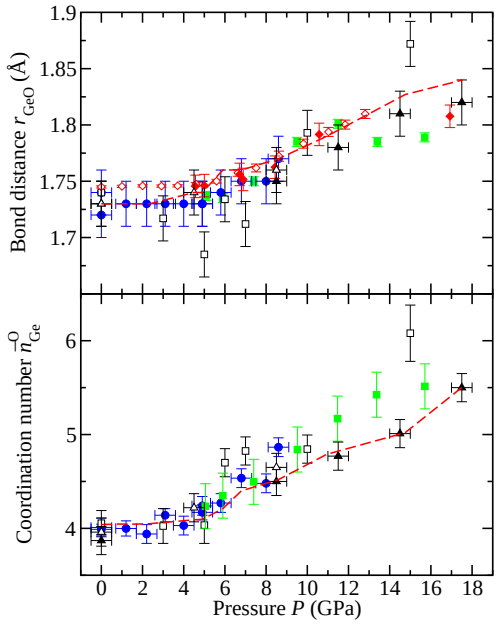

Figure 14. The pressure dependence of (a) the Ge-O bond length r_{GeO} and (b) the mean coordination number $\bar{n}^{O}_{Ge}$ for GeO_2 glass as measured in the present work by using neutron diffraction with either single (△) or double (▲) toroid anvils. The bond distances were obtained from the position of the first peak in $G(r)$ while the $\bar{n}^{O}_{Ge}$ values were obtained by integrating over this peak to the first minimum (see equation (5)). The results are compared to those obtained from the previous neutron diffraction experiments of Drewitt *et al* [17] [(blue) ●], the x-ray diffraction experiments of Guthrie *et al* [13] (□) and Mei *et al* [18] [(green) ■], and the EXAFS experiments of Vaccari *et al* [16] [(red) ◊] and Baldini *et al* [19] [(red) ♦]. The broken (red) curves show the molecular dynamics results obtained by using the DIPPIM interaction potentials for the weighted average $\langle r_{GeO} \rangle$ (see the text) and $\bar{n}^{O}_{Ge}$ as obtained by integrating over the first peak in $g_{GeO}(r)$ to the first minimum.

the neutron diffraction data and there is a reduction in dQ_{FSDP}/dP starting around 8 GPa (figure 13). The pressure range from about 4.5 to 8 GPa corresponds to a mass density increase from about 4.25 to 5.02 g cm^{-3} and, according to the molecular dynamics results shown in the inset to figure 15(b), this corresponds to a regime where the predominant conversion mechanism is from four-fold to five-fold coordinated Ge atoms. The occurrence in germania of GeO_5 units at pressures $\geq$ 5 GPa is supported by recent inelastic x-ray scattering experiments made at the oxygen K-edge [73]. For densities greater that 5.25 g cm^{-3} ($P \gtrsim 10$ GPa) six-fold coordinated Ge atoms start to appear in appreciable concentrations ($\gtrsim 10\%$). This picture for the densification mechanisms in glassy GeO_2, indicated by the agreement found at the total structure factor level between the diffraction and molecular dynamics results, is supported by a comprehensive and quantitative structural investigation involving the method of neutron diffraction with Ge isotope substitution at pressures up to 8 GPa [74].

In figure 15, the density dependence of the Ge-O bond distance and coordination number from the molecular-dynamics simulations using the DIPPIM interaction

potentials are compared with the results obtained from other simulations of GeO_2 glass using either molecular dynamics and the Oeffner-Elliott interaction potentials [38, 39, 40, 41, 72] or first principles molecular dynamics [42]. Often, the former do not give a self consistent view of the structure which is attributable, at least in part, to different parameterizations of the Oeffner-Elliott potentials [36, 37]. For example, Micoulaut and co-workers [38, 39] found that r_{GeO} remains constant at 1.73 Å as the density increases from ambient to 5.5 g cm^{-3} and $\bar{n}^{\mathrm{O}}_{\mathrm{Ge}}$ increases from $\simeq$4.1 to $\simeq$4.9 whereas Shanavas *et al* [40] found an almost linear increase of r_{GeO} from 1.78 to 1.83 Å as the density increases from ambient to 5.5 g cm^{-3} and $\bar{n}^{\mathrm{O}}_{\mathrm{Ge}}$ increases from 4 to $\simeq$5.1. Both descriptions of the pressure dependence of the structure of GeO_2 glass are, however, in contrast with the experimental results (figure 14). In comparison, the first principles molecular-dynamics simulations of Zhu and Chen [42], made using a system containing 108 atoms, found an elongated Ge-O bond length of 1.80 Å at ambient pressure which increases to 1.81 Å as the density is increased to 4.27 g cm^{-3} and which then increases rapidly to 1.89 Å as the density is increased further to 5.4 g cm^{-3}. The mean Ge-O coordination number is, however, steady at $\bar{n}^{\mathrm{O}}_{\mathrm{Ge}} \simeq 4$ as the density is increased to 5.4 g cm^{-3} but then increases rapidly to $\simeq$5.8 as the density is increased to 5.66 g cm^{-3}. Again, this behavior is not observed experimentally (figure 14) and might be a consequence of the very small number of simulated atoms. In summary, only those molecular-dynamics simulations made using the DIPPIM interaction potentials give a good account of the experimental results obtained for r_{GeO} and $\bar{n}^{\mathrm{O}}_{\mathrm{Ge}}$ from several different experimental methods.

7.3. Density dependence of the structures of GeO_2 and SiO_2

Finally, it is of interest to compare the pressure dependence of the structures of GeO_2 and SiO_2 glass. Under ambient conditions both of these materials form networks constructed from corner sharing MO_4 tetrahedra with mean inter-tetrahedral M-O-M bond angles of 132(2)° [24] and 151° [5], respectively, where M denotes Ge or Si. With increasing density, SiO_2 is also converted from a tetrahedral to an octahedral glass, the changes occurring at higher pressures by comparison to GeO_2 [10, 14, 21]. As shown in figure 16, the structural changes do, however, occur at similar scaled number densities $\rho\bar{r}^3_{\mathrm{MO}}$, where ρ was taken from Ref. [50] in the case of GeO_2 or from Refs. [15] and [75] in the case of SiO_2, and $\bar{r}_{\mathrm{MO}}$ is the M-O bond length at ambient pressure. For example, in both GeO_2 and SiO_2 the bond length r_{MO} and coordination number $\bar{n}^{\mathrm{O}}_{\mathrm{M}}$ remain constant at low pressures but then increase once the dimensionless number density $\rho\bar{r}^3_{\mathrm{MO}} \gtrsim 0.4$. There is also a change in the gradient dQ_{FSDP}/dP for both glasses at $\rho\bar{r}^3_{\mathrm{MO}} \simeq 0.45$.

As discussed in section 7.2, in the case of GeO_2 the regime where $\rho\bar{r}^3_{\mathrm{MO}} \lesssim 0.4$ is associated with a reorganization of GeO_4 units, the regime where $0.4 \lesssim \rho\bar{r}^3_{\mathrm{MO}} \lesssim 0.45$ corresponds to a predominant replacement of GeO_4 units by GeO_5 units, and the regime where $\rho\bar{r}^3_{\mathrm{MO}} \gtrsim 0.45$ corresponds to the appearance of appreciable concentrations of GeO_6 units. Thus in the case of SiO_2, similar structural transformations are

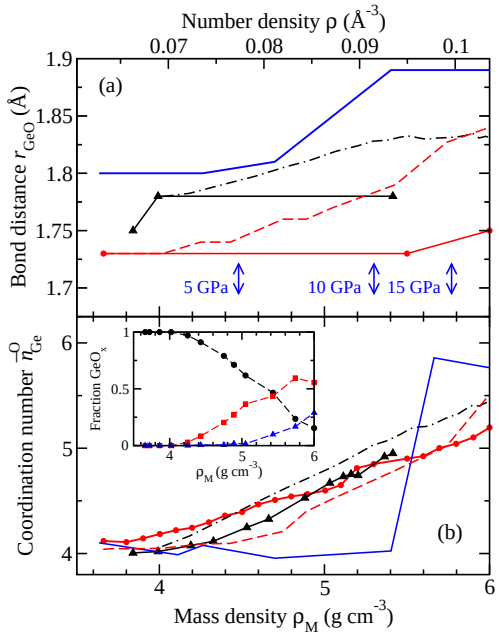

Figure 15. The density dependence of (a) the Ge-O bond length r_{GeO} and (b) the mean coordination number $\bar{n}^{\mathrm{O}}_{\mathrm{Ge}}$ for GeO_2 glass as obtained from molecular-dynamics simulations using the DIPPIM interaction potentials (broken light (red) curves), the molecular-dynamics simulations of Micoulaut *et al* [38, 39] (solid (red) curves with circles), Shanavas *et al* [40] (chained dark (black) curves) and Li *et al* [41] (solid (black) curves with triangles) using the Oeffner-Elliott interaction potentials [72], and the first principles molecular-dynamics simulations of Zhu and Chen [42] (solid dark (blue) curves). The vertical arrows mark the densities corresponding to 5, 10 and 15 GPa. The inset in (b) shows the density dependence of the fraction of GeO_x species, where $x = 4$ (●), 5 [(red) ■] or 6 [(blue) ▲], calculated using the DIPPIM interaction potentials.

anticipated e.g. SiO_4 units are expected to be replaced predominantly by SiO_5 units in a dimensionless number density regime for which the pressure ranges from about 15 to 24 GPa. These findings are in broad agreement with the molecular dynamics study of dense SiO_2 by Liang *et al* [76] and with a recent first principles molecular dynamics study by Wu *et al* [77]. X-ray Raman scattering (XRS) oxygen K-edge spectra show little change at pressures below 14 GPa and may be interpreted at higher pressures in terms of the formation of SiO_5 units [77, 78]. The appearance of SiO_5 units at pressures above 12 GPa has also been suggested on the basis of XRS silicon L-edge spectra [79].

In figure 17(a), the structure factor $S(Q)$ measured for GeO_2 glass at ambient pressure by using neutron diffraction [23, 24] is compared to the $S(Q)$ measured for SiO_2 glass at ambient pressure by using x-ray diffraction [80]. Here, the structure factors are defined by $S(Q) = 1 + F(Q)/\langle b(Q)\rangle^2$ where $F(Q)$ is given by equation (1), albeit with Q dependent scattering lengths (or form factors) in the case of x-ray diffraction experiments, and the mean scattering length $\langle b(Q)\rangle = c_{\mathrm{M}} b_{\mathrm{M}}(Q) + c_{\mathrm{O}} b_{\mathrm{O}}(Q)$. The weighting factors for the Ge-Ge, Ge-O and O-O partial structure factors in $S(Q)$ for

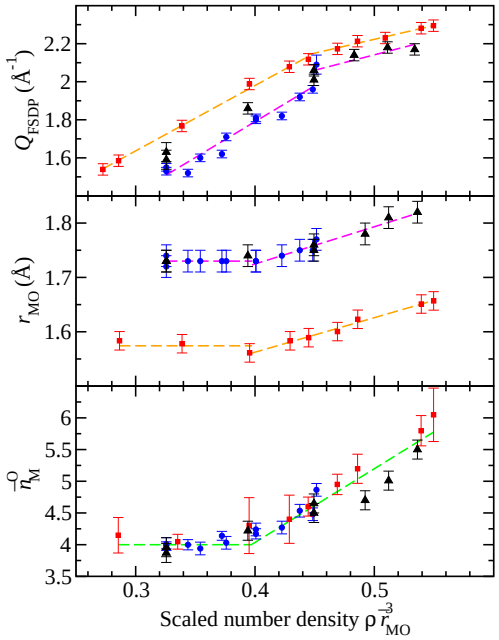

Figure 16. The dependence on the scaled number density $\rho\bar{r}^3_{\rm MO}$ of (a) the position of the first sharp diffraction peak $Q_{\rm FSDP}$ in the measured total structure factor for GeO_2 or SiO_2, (b) the bond distance $r_{\rm MO}$ as deduced from the position of the first peak in the total pair distribution function where M denotes Ge or Si, and (c) the coordination number $\bar{n}^{\rm O}_{\rm M}$. In the expression $\rho\bar{r}^3_{\rm MO}$ the values $\bar{r}_{\rm GeO} = 1.73$ Å and $\bar{r}_{\rm SiO} = 1.60$ Å were used [23]. The neutron diffraction results for GeO_2 were taken from Ref. [17] [(blue) ●] and the present work (▲) while the x-ray diffraction results for SiO_2 were taken from Ref. [20] [(red) ■]. The broken straight lines are fits to the data sets at either small or large densities.

a neutron diffraction experiment on GeO_2 glass are in the ratio 0.1710:0.4851:0.3439 while the weighting factors for the Si-Si, Si-O and O-O partial structure factors in $S(Q)$ for an x-ray diffraction experiment on SiO_2 glass are in the ratio 0.2178:0.4978:0.2844 at $Q = 0$. Corresponding partial structure factors therefore receive similar weighting factors such that only large discrepancies between the neutron $S(Q)$ for GeO_2 glass and the x-ray $S(Q)$ for SiO_2 glass are likely to arise from substantial differences between the structures of these materials, as in the region of the FSDP at ambient pressure (figure 17(a)) [23, 24]. In figure 17(b), the neutron $S(Q)$ for GeO_2 glass at 17.5 GPa ($\rho\bar{r}^3_{\rm GeO} = 0.536$) where $\bar{n}^{\rm O}_{\rm Ge} = 5.5(2)$ is compared to the x-ray $S(Q)$ for SiO_2 glass as measured for pressures of 43.5 GPa ($\rho\bar{r}^3_{\rm SiO} = 0.550$) where $\bar{n}^{\rm O}_{\rm Si} = 6.0(4)$ [20] and 50 GPa ($\rho\bar{r}^3_{\rm SiO} = 0.573$) where $\bar{n}^{\rm O}_{\rm Si} \simeq 6.3$ [15]. The functions show similar overall features which are therefore indicative of the formation of a substantial fraction of MO_5 and/or MO_6 units in both materials.

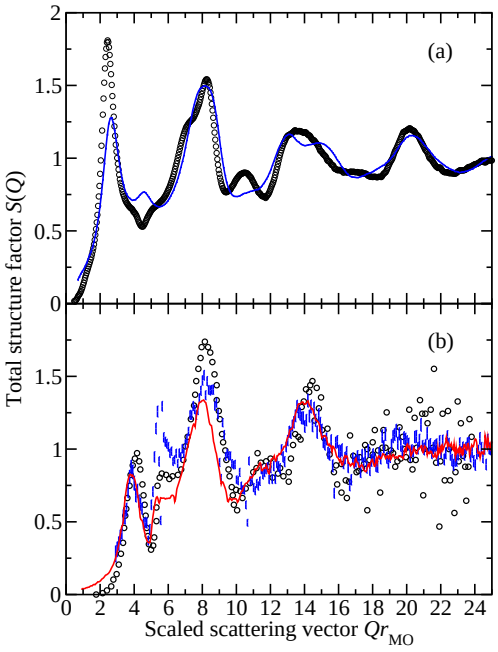

Figure 17. The total structure factor $S(Q)$ measured for GeO_2 or SiO_2 glass using neutron or x-ray diffraction, plotted as a function of the scaled scattering vector Qr_{MO} where r_{MO} is the Ge-O or Si-O bond distance at the relevant pressure. (a) The x-ray diffraction $S(Q)$ as measured at ambient pressure for SiO_2 glass (r_{SiO} = 1.60 Å) (open circles) [80] compared to the neutron diffraction $S(Q)$ as measured at ambient pressure for GeO_2 glass of natural isotopic abundance (r_{GeO} = 1.73 Å) (solid (blue) curve) [23, 24]. (b) The x-ray diffraction $S(Q)$ as measured for SiO_2 glass at 43.5 GPa (r_{SiO} = 1.66 Å) (solid light (red) curve) [20] or at 50 GPa (r_{SiO} = 1.71 Å) (open circles) [15] compared to the neutron diffraction $S(Q)$ as measured for GeO_2 glass at 17.5 GPa (r_{GeO} = 1.82 Å) (points with vertical (blue) error bars).

7.4. Geophysical implications

Germania and germanates are often regarded as structural analogues of silica and silicates, where structural transformations in the former occur at lower pressures than in the latter, making them more amenable to study by *in situ* experimental methods [14]. For example, crystalline GeO_2 and SiO_2 can both exhibit the same sequence of pressure and temperature-driven structural transformations but, in the case of germania, these occur under less extreme conditions [81]. Accordingly, the pressure and temperature-driven structural transformations in Mg_2GeO_4 have been extensively investigated to study e.g. the phase transition between polymorphs with the olivine and spinel structures and the mechanical properties of these polymorphs [82, 83, 84, 85, 86]. The germanate Mg_2GeO_4 is an analogue of fosterite Mg_2SiO_4 which is the Mg rich member of the olivine solid solution series $(Mg,Fe)_2SiO_4$, important constituents of the Earth's upper mantle [87].

The observed transformations for GeO_2 glass occur at similar dimensionless number densities to those found for SiO_2 glass, indicating e.g. a regime from about 15 to

24 GPa where SiO_4 units are replaced predominantly by SiO_5 units and a regime beyond ∼24 GPa where appreciable concentrations of SiO_6 units begin to form. As the glass can explore localities on an energy landscape that are inaccessible to the crystalline state, the behaviour we observe may give new insight into the atomic configurations of the compressed high-temperature liquid that are not accessible by crystallographic studies. This could have geophysical implications because silicates account for a significant proportion of the Earth's mantle, and structural changes that take place under high-pressure and temperature conditions alter physical properties (e.g. the compressibility, thermal expansivity and viscosity) that govern magma related processes such as volcanic activity and the differentiation and evolution in composition of the planetary interior [88, 89]. Although planetary systems are substantially more complex than those studied here (in terms e.g. of chemical composition, temperature and oxygen fugacity), even relatively simple liquid silicates are difficult to probe by experiment [90]. As suggested by molecular dynamics simulations [91, 92], the formation of SiO_5 species in these liquids is likely to have a substantial impact on the extent of network polymerisation and, thereby, the physical properties of the melt.

8. Conclusions

Neutron diffraction was used to measure the structure of GeO_2 glass at pressures up to 17.5(5) GPa with a PE press and sintered diamond anvils. The new methodology that has been developed leads to corrected diffraction patterns that are largely free from diamond Bragg peaks and its validity has been verified by comparison with the data available from other neutron diffraction experiments at pressures up to ≃8.5 GPa. The neutron structure factors thus obtained are the highest quality ever measured above ∼9 GPa which offers the opportunity for studying the detailed structure of glassy and liquid materials by using neutron diffraction over an elevated range of pressures.

The new diffraction and molecular dynamics results for GeO_2 glass are consistent with the existence of four principal densification mechanisms. At pressures up to a threshold of ≃5 GPa the density increases through a change in the connectivity of GeO_4 tetrahedra [17]. At pressures beyond this threshold, there is a steady increase in the Ge-O bond length and coordination number in contrast with an early EXAFS study [9] but in agreement with more recent neutron and x-ray diffraction and EXAFS experiments [16, 17, 18]. The rate of change of the intermediate-range order, as measured by the pressure dependence of $Q_{\rm FSDP}$, decreases once the pressure exceeds ∼10 GPa and the Ge-O coordination number $\bar{n}^{\rm O}_{\rm Ge} > 4.5$. According to the molecular dynamics results obtained by using the DIPPIM interaction potentials, the pressure range from 5 to ∼10 GPa corresponds to a regime where GeO_4 units are replaced predominantly by GeO_5 units and, at pressures beyond ∼10 GPa, appreciable concentrations of GeO_6 units begin to form. The occurrence of GeO_5 units at pressures $\geq$ 5 GPa is supported by recent inelastic x-ray scattering experiments [73] and by a detailed structural investigation using the method of Ge isotope substitution in neutron diffraction [74]. Eventually, at

about 30 GPa, the transformation to a predominantly octahedral glass is achieved and densification proceeds via compression of the Ge-O bond [19]. The onset of two of these densification regimes correspond to observable changes in the pressure dependence of the bulk number density of the glass ρ which shows an increase in $d\rho/dP$ at $\simeq$5 GPa followed by a decrease in $d\rho/dP$ at $\simeq$10 GPa (figure 1).

The observed transformations for GeO_2 glass occur at similar dimensionless number densities to those found for SiO_2 glass, indicating e.g. a regime from about 15 to 24 GPa where SiO_4 units are replaced predominantly by SiO_5 units and a regime beyond $\sim$24 GPa where appreciable concentrations of SiO_6 units begin to form.

Acknowledgments

We thank Duncan Francis and Chris Barry (ISIS) for help with the neutron diffraction experiments, Stefan Klotz (Paris) for helpful discussions on the pressure calibration curves, for providing several of his data sets, and for refining the NaCl data taken in the $GeSe_2$-NaCl pressure calibration run, Henry-Fischer (ILL, Grenoble) for help in acquiring several of the data points for the calibration curves for single toroid anvils, Alex Hannon (ISIS) for help in calculating the inelasticity corrections, and Mathieu Salanne (Paris) for helpful discussions on GeO_2. We are also grateful to Chris Benmore (APS) and Qiang Mei (NIU) for providing their x-ray diffraction results. The EPSRC (award EP/G008795/1) and STFC Centre for Materials Physics and Chemistry (award CMPC08105) are thanked for financial support. DM wishes to thank the Government of Ireland for an EMPOWER Postdoctoral Fellowship and the Trinity Centre for High Performance Computing for computing time.

The Gd shielding arrangement was developed during an experiment on SiO_2 by Wilding, Guthrie, Bull, Tucker and Salmon. The experiments on GeO_2 were made by Drewitt, Salmon, Bull, Tucker, Whittaker, Wezka and Guthrie during which the vanadium normalization protocol was developed by Drewitt, Salmon, Guthrie, Bull and Tucker. The attenuation corrections were derived by Salmon and Zeidler (who also constructed figure 16), the diffraction data were analyzed by Drewitt and Whittaker, and the method for dealing with the absence of small Q data was developed by Drewitt, Whittaker and Salmon. The pressure calibration curves were finalized by Whittaker after input from Bull, Drewitt, Guthrie, Salmon, Tucker, Wezka and Zeidler and with help from Klotz and Fischer (see above). The molecular-dynamics simulations were made by Marrocchelli.

Appendix A. Evaluating the attenuation coefficient

Consider an incident beam of intensity $I_0(Q)$ and circular cross-section of radius R_B which lies parallel to the Z axis of a Cartesian coordinate system (figure 5). The incident intensity depends on Q because the scattering angle is fixed at $2\theta \simeq 90^\circ$ but the incident wavelength is variable such that $Q \simeq 2\sqrt{2}\pi/\lambda$. Let the beam impinge

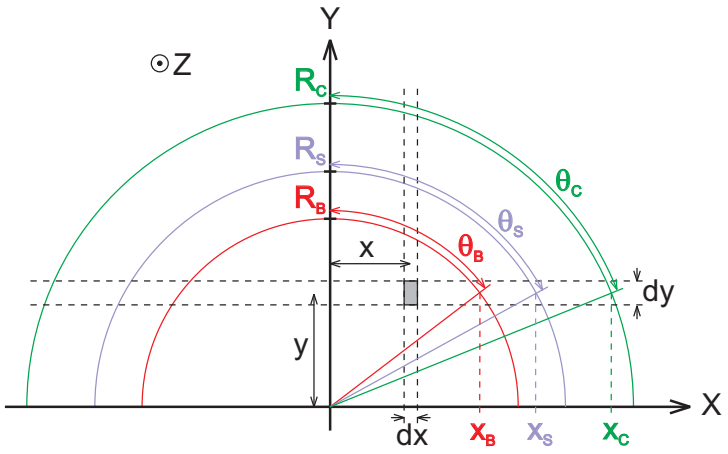

Figure A1. A cut in the X-Y plane taken through the sample and gasket assembly perpendicular to an incident neutron beam which lies parallel to the Z axis. The cut is of thickness dz at a distance z below the illuminated top surface of the sample and the incident beam impinges on an element of sample with volume $dV = dxdydz$ that forms part of a strip of width dy at y. The beam, sample and outer container radii are denoted by R_B, R_S and R_C, respectively, and the intercepts of the strip with these radii correspond to X axis values of x_B, x_S and x_C, respectively. The intercepts define angles of θ_B, θ_S and θ_C relative to the Y axis.

on a cylindrical sample of radius $R_S > R_B$ and height h contained within an annular container (or gasket) of outer radius $R_C > R_S$ and height h such that Z is the axis of symmetry and the scattered beam lies in the X-Y plane (figure A1). Let the origin of coordinates lie at the center of the illuminated top surface of the sample and consider a thin strip in the X-Y plane at a depth z where the width of the strip is dy at y and its thickness is dz. By reference to figure A1, $y = R_B \cos\theta_B$, $x_S = R_S \sin\theta_S$ and, since $\cos\theta_S = y/R_S = R_B \cos\theta_B/R_S$ and $\cos^2\theta_S + \sin^2\theta_S = 1$, it follows that

$$x_S = \left(R_S^2 - R_B^2 \cos^2\theta_B\right)^{1/2}. \tag{A.1}$$

Similarly, $x_C = R_C \sin\theta_C$ and, given that $\cos\theta_C = y/R_C = R_B \cos\theta_B/R_C$ and $\cos^2\theta_C + \sin^2\theta_C = 1$, it follows that

$$x_C = \left(R_C^2 - R_B^2 \cos^2\theta_B\right)^{1/2}. \tag{A.2}$$

Consider the scattering from an illuminated element of the sample within the strip which has a volume $dV = dxdydz$. Let μ_S and μ_C be the attenuation coefficients of the sample and container, respectively, and let ρ_S be the atomic number density of the sample. Then, if the single scattered intensity per sample atom is $I_S(Q)$, the observed intensity from the illuminated volume element is given by

$$dI(Q) = I_0(Q)\exp(-\mu_S z)\,dxdydz\,\rho_S\,I_S(Q)\exp[-\mu_S(x_S - x)]\exp[-\mu_C(x_C - x_S)]. \tag{A.3}$$

The observed intensity for scattering by the entire illuminated strip is found by integrating equation (A.3) from $x = -R_B \sin\theta_B$ to $x = R_B \sin\theta_B$ and is given by

$$\begin{aligned} I_{\rm strip}(Q) = {} & I_0(Q)\exp(-\mu_S z)\,dydz\,\rho_S\,I_S(Q)\ \times \\ & \times\ \exp[-\mu_C(x_C - x_S)]\exp(-\mu_S x_S)\,(2/\mu_S)\sinh(\mu_S R_S \sin\theta_B). \end{aligned} \tag{A.4}$$

The observed intensity for single scattering by the entire disc is found by integrating equation (A.4) from $y = 0$ to $y = R_B$ and by using the symmetry of the set-up to double the result. On making the change of variable $dy = -R_B \sin\theta_B d\theta_B$ it follows that

$$I_{\rm disc}(Q) = I_0(Q) \exp(-\mu_S z)\, dz\, \rho_S\, I_S(Q)(4R_B/\mu_S) \int_0^{\pi/2} d\theta_B \sin\theta_B f(\theta_B) \tag{A.5}$$

where

$$f(\theta_B) = \exp[-(\mu_S - \mu_C)x_S] \exp(-\mu_C x_C) \sinh(\mu_S R_S \sin\theta_B), \tag{A.6}$$

x_S is given by given by equation (A.1) and x_C is given by equation (A.2). The observed intensity for single scattering by the entire sample is found by integrating equation (A.5) from $z = 0$ to $z = h$ such that

$$I_{SC}(Q) = I_0(Q)\,[1 - \exp(-\mu_S h)]\,\rho_S\, I_S(Q)(4R_B/\mu_S^2) \int_0^{\pi/2} d\theta_B \sin\theta_B f(\theta_B). \tag{A.7}$$

In the absence of attenuation the total intensity for single scattering from the sample would be given by

$$I_S^{\rm tot}(Q) = I_0(Q)\,\pi R_B^2 h\,\rho_S\, I_S(Q). \tag{A.8}$$

In practice, beam attenuation reduces this intensity such that $I_{SC}(Q) = A_{S,SC}(Q) I_S^{\rm tot}(Q)$. Thus the attenuation coefficient, corresponding to scattering by the sample and attenuation by the sample and its container, is given by

$$A_{S,SC}(Q) = \frac{4}{\pi R_B h} \frac{[1 - \exp(-\mu_S h)]}{\mu_S^2} \int_0^{\pi/2} d\theta_B \sin\theta_B f(\theta_B) \tag{A.9}$$

where the Q dependence arises because the attenuation coefficients μ_S and μ_C depend on the incident wavelength λ and, for the scattering geometry, $Q \simeq 2\sqrt{2}\pi/\lambda$. In the small-sample limit when $\mu_S \to 0$ and $\mu_C \to 0$, $\sinh(\mu_S R_S \sin\theta_B) \to \mu_S R_S \sin\theta_B$ and the attenuation coefficient $A_{S,SC}(Q) \to 1$ as required.

References

[1] Angell C A 1995 *Science* **267** 1924
[2] Wright A C, Etherington G, Desa J A E, Sinclair R N, Connell G A N, and Mikkelsen Jr J C 1982 *J. Non-Cryst. Solids* **49** 63
[3] Galeener F L, Leadbetter A J and Stringfellow M W 1983 *Phys. Rev. B* **27** 1052
[4] Wright A C, Clare A G, Etherington G, Sinclair R N, Brawer S A and Weber M J 1989 *J. Non-Cryst. Solids* **111** 139
[5] Tucker M G, Keen D A, Dove M T and Trachenko K 2005 *J. Phys.: Condens. Matter* **17** S67
[6] Salmon P S 2007 *J. Phys.: Condens. Matter* **19** 455208
[7] Wilson M and Salmon P S 2009 *Phys. Rev. Lett.* **103** 157801
[8] Williams Q and Jeanloz R 1988 *Science* **239** 902
[9] Itié J P, Polian A, Calas G, Petiau J, Fontaine A and Tolentino H 1989 *Phys. Rev. Lett.* **63** 398
[10] Durben D J and Wolf G H 1991 *Phys. Rev. B* **43** 2355
[11] Madon M, Gillet Ph, Julien Ch and Price G D 1991 *Phys. Chem. Minerals* **18** 7
[12] Meade C, Hemley R J and Mao H K 1992 *Phys. Rev. Lett.* **69** 1387
[13] Guthrie M, Tulk C A, Benmore C J, Xu J, Yarger J L, Klug D D, Tse J S, Mao H -k and Hemley R J 2004 *Phys. Rev. Lett.* **93** 115502

[14] Micoulaut M, Cormier L and Henderson G S 2006 *J. Phys.: Condens. Matter* **18** R753
[15] Sato T and Funamori N 2008 *Phys. Rev. Lett.* **101** 255502
[16] Vaccari M, Aquilanti G, Pascarelli S and Mathon O 2009 *J. Phys.: Condens. Matter* **21** 145403
[17] Drewitt J W E, Salmon P S, Barnes A C, Klotz S, Fischer H E and Crichton W A 2010 *Phys. Rev. B* **81** 014202
[18] Mei Q, Sinogeikin S, Shen G, Amin S, Benmore C J and Ding K 2010 *Phys. Rev. B* **81** 174113
[19] Baldini M, Aquilanti G, Mao H -k, Yang W, Shen G, Pascarelli S and Mao W L 2010 *Phys. Rev. B* **81** 024201
[20] Benmore C J, Soignard E, Amin S A, Guthrie M, Shastri S D, Lee P L and Yarger J L 2010 *Phys. Rev. B* **81** 054105
[21] Polsky C H, Smith K H and Wolf G H 1999 *J. Non-Cryst. Solids* **248** 159
[22] Fischer H E, Barnes A C and Salmon P S 2006 *Rep. Prog. Phys.* **69** 233
[23] Salmon P S, Barnes A C, Martin R A and Cuello G J 2006 *Phys. Rev. Lett.* **96** 235502
[24] Salmon P S, Barnes A C, Martin R A and Cuello G J 2007 *J Phys.: Condens. Matter* **19** 415110
[25] Penfold I T and Salmon P S 1991 *Phys. Rev. Lett.* **67** 97
[26] Petri I, Salmon P S and Fischer H E 2000 *Phys. Rev. Lett.* **84** 2413
[27] Salmon P S and Petri I 2003 *J. Phys.: Condens. Matter* **15** S1509
[28] Salmon P S, Martin R A, Mason P E and Cuello G J 2005 *Nature* **435** 75
[29] Zeidler A, Salmon P S, Martin R A, Usuki T, Mason P E, Cuello G J, Kohara S and Fischer H E 2010 *Phys. Rev. B* **82** 104208
[30] Klotz S, Strässle Th, Rousse G, Hamel G and Pomjakushin V 2005 *Appl. Phys. Lett.* **86** 031917
[31] Zeidler A, Drewitt J W E, Salmon P S, Barnes A C, Crichton W A, Klotz S, Fischer H E, Benmore C J, Ramos S and Hannon A C 2009 *J. Phys.: Condens. Matter* **21** 474217
[32] Wilding M, Guthrie M, Bull C L, Tucker M G and McMillan P F 2008 *J. Phys.: Condens. Matter* **20** 244122
[33] Wilding M, Guthrie M, Kohara S, Bull C L, Akola J and Tucker M G 2012 *J. Phys.: Condens. Matter* **24** 225403
[34] Wilding M, Guthrie M, Kohara S, Bull C L, Akola J and Tucker M G 2012 *J. Phys.: Condens. Matter* **24** 339501
[35] Besson J M, Pruzan Ph, Klotz S, Hamel G, Silvi B, Nelmes R J, Loveday J S, Wilson R M and Hull S 1994 *Phys. Rev. B* **49** 12540
[36] Marrocchelli D, Salanne M, Madden P A, Simon C and Turq P 2009 *Mol. Phys.* **107** 443
[37] Marrocchelli D, Salanne M and Madden P A 2010 *J. Phys.: Condens. Matter* **22** 152102
[38] Micoulaut M 2004 *J. Phys.: Condens. Matter* **16** L131
[39] Micoulaut M, Guissani Y and Guillot B 2006 *Phys. Rev. E* **73** 031504
[40] Shanavas K V, Garg N and Sharma S M 2006 *Phys. Rev. B* **73** 094120
[41] Li T, Huang S and Zhu J 2009 *Chem. Phys. Lett.* **471** 253
[42] Zhu X F and Chen L F 2009 *Physica B* **404** 4178
[43] Faber T E and Ziman J M 1965 *Phil. Mag.* **11** 153
[44] Sears V F 1992 *Neutron News* **3** (Number 3) 26
[45] Salmon P S 2005 *J. Phys.: Condens. Matter* **17** S3537
[46] Salmon P S 2006 *J. Phys.: Condens. Matter* **18** 11443
[47] Bhatia A B and Thornton D E 1970 *Phys. Rev. B* **2** 3004
[48] Klotz S, Besson J M, Hamel G, Nelmes R J, Loveday J S, Marshall W G and Wilson R M 1995 *Appl. Phys. Lett.* **66** 1735
[49] Bull C L, Guthrie M, Klotz S, Philippe J, Strässle Th, Nelmes R J, Loveday J S and Hamel G 2005 *High Press. Res.* **25** 229
[50] Hong X, Shen G, Prakapenka V B, Newville M, Rivers M L and Sutton S R 2007 *Phys. Rev. B* **75** 104201
[51] Smith K H, Shero E, Chizmeshya A and Wolf G H 1995 *J. Chem. Phys.* **102** 6851
[52] Tsiok O B, Brazhkin V V, Lyapin A G and Khvostantsev L G 1998 *Phys. Rev. Lett.* **80** 999

[53] Nakamoto Y, Takemura K, Ishizuka M, Shimizu K and Kikegawa T *Equation of State for Vanadium under Hydrostatic Conditions* presented at the Joint 20th AIRAPT (International Association for the Advancement of High Pressure Science and Technology) − 43rd EHPRG (European High Pressure Research Group) meeting, June 27 − July 1, Karlsruhe, Germany (2005).
[54] Marshall W G and Francis D J 2002 *J. Appl. Cryst.* **35** 122
[55] Brown J M 1999 *J. Appl. Phys.* **86** 5801
[56] Hemley R J, Jephcoat A P, Mao H K, Zha C S, Finger L W and Cox D E 1987 *Nature* **330** 737
[57] Klotz S, Steinle-Neumann G, Strässle Th, Philippe J, Hansen Th and Wenzel M J 2008 *Phys. Rev. B* **77** 012411
[58] Martínez-García D, Le Godec Y, Mézouar M, Syfosse G, Itié J P and Besson J M 2000 *High Press. Res.* **18** 339
[59] Le Bail A, Duroy H and Fourquet J L 1988 *Mater. Res. Bull.* **23** 447
[60] Madden P A, Heaton R, Aguado A and Jahn S 2006 *J. Mol. Struct.: Theochem* **771** 9
[61] Burbano M, Marrocchelli D, Yildiz B, Tuller H L, Norberg S T, Hull S, Madden P A and Watson G W 2011 *J. Phys.: Condens. Matter* **23** 255402
[62] Norberg S T, Hull S, Ahmed I, Eriksson S G, Marrocchelli D, Madden P A, Li P and Irvine J T S 2011 *Chem. Mater.* **23** 1356
[63] Liang Y, Miranda C R and Scandolo S 2008 *High Pressure Res.* **28** 35
[64] Howe M A, McGreevy R L and Howells W S 1989 *J. Phys.: Condens. Matter* **1** 3433
[65] Soper A K and Egelstaff P A 1980 *Nucl. Instrum. Meth.* **178** 415
[66] Bolef D I, Smith R E and Miller J G 1971 *Phys. Rev. B* **3** 4100
[67] Suito K, Miyoshi M, Sasakura T and Fujisawa H 1992 *High-Pressure Research: Applications to Earth and Planetary Sciences* ed Y Syono and M H Manghnani (Washington DC, American Geophysical Union) p 219
[68] Sokolov A P, Kisliuk A, Soltwisch M and Quitmann D 1992 *Phys. Rev. Lett.* **69** 1540
[69] Salmon P S 1994 *Proc. R. Soc. Lond. A* **445** 351
[70] Shen G, Mei Q, Prakapenka V B, Lazor P, Sinogeikin S, Meng Y and Park C 2011 *Proc. Natl. Acad. Sci.* **108** 6004
[71] Sato T, Funamori N and Yagi T 2011 *Nature Commun.* **2** 345
[72] Oeffner R D and Elliott S R 1998 *Phys. Rev. B* **58** 14791
[73] Lelong G, Cormier L, Ferlat G, Giordano V, Henderson G S, Shukla A and Calas G 2012 *Phys. Rev. B* **85** 134202
[74] Wezka K, Salmon P S, Zeidler A, Whittaker D A J, Drewitt J W E, Klotz S, Fischer H E and Marrocchelli D (in preparation).
[75] Meade C and Jeanloz R 1987 *Phys. Rev. B* **35** 236
[76] Liang Y, Miranda C R and Scandolo S 2007 *Phys. Rev. B* **75** 024205
[77] Wu M, Liang Y, Jiang J-Z and Tse J S 2012 *Sci. Rep.* **2** 398
[78] Lin J-F, Fukui H, Prendergast D, Okuchi T, Cai Y Q, Hiraoka N, Yoo C-S, Trave A, Eng P, Hu M Y and Chow P 2007 *Phys. Rev. B* **75** 012201
[79] Fukui H, Kanzaki M, Hiraoka N and Cai Y Q 2008 *Phys. Rev. B* **78** 012203
[80] Kohara S, Itou M, Suzuya K, Inamura Y, Sakurai Y, Ohishi Y and Takata M 2007 *J. Phys.: Condens. Matter* **19** 506101
[81] Prakapenka V P, Shen G, Dubrovinsky L S, Rivers M L and Sutton S R 2004 *J. Phys. Chem. Solids* **65** 1537
[82] Ringwood A E 1956 *Am. J. Sci.* **254** 707
[83] Ross N L and Navrotsky A 1987 *Phys. Chem. Mineral.* **14** 473
[84] Burnley P C, Green II H W and Prior D J 1991 *J. Geophys. Res.* **96** 425
[85] Reynard B, Petit P-E, Guyot F and Gillet P 1994 *Phys. Chem. Mineral.* **20** 556
[86] Burnley P C 2005 *Am. Mineral.* **90** 1315
[87] Walther J V 2005 *Essentials of Geochemistry* (Sudbury MA: Jones and Bartlett)
[88] Poirier J-P 2000 *Introduction to the Physics of the Earth's Interior* 2nd ed (Cambridge: Cambridge

University Press)
[89] Anderson D L 2007 *New Theory of the Earth* (Cambridge: Cambridge University Press)
[90] Funamori N, Yamamoto S, Yagi T and Kikegawa T 2004 *J. Geophys. Res.* **109**, B03203
[91] Angell C A, Cheeseman P A and Tamaddon S 1982 *Science* **218** 885
[92] Kubicki J D and Lasaga A C 1991 *Phys. Chem. Mineral.* **17** 661